



Research Papers

GO/ZnO-based all-solid-state photo-supercapacitors: Effect of GO:ZnO ratio on composite properties and device performance

Cigdem Tuc Altas^a, Tuluhan Olcayto Colak^b, Arpad Mihai Rostas^c, Maria Mihet^c,
Mihaela Diana Lazar^c, Igor Iatsunskiy^d, Emerson Coy^d, Ipek Deniz Yildirim^e,
Feryal Bakan Misirlioglu^e, Emre Erdem^e, Mehmet Sankir^{a,b,*}, Nurdan Demirci Sankir^{a,b,*}

^a Department of Materials Science and Nanotechnology Engineering, TOBB University of Economics and Technology, Sogutozu Caddesi No 43 Sogutozu, 06560 Ankara, Turkey

^b Micro and Nanotechnology Graduate Program, TOBB University of Economics and Technology, Sogutozu Caddesi No 43 Sogutozu, 06560 Ankara, Turkey

^c National Institute for Research and Development of Isotopic and Molecular Technologies-INCITIM, 67-103 Donat, 400293 Cluj-Napoca, Romania

^d NanoBioMedical Centre, Adam Mickiewicz University in Poznań, Wszechnicy Piastowskiej 3, 61-614 Poznań, Poland

^e Faculty of Engineering and Natural Sciences, Sabanci University, Orhanli, Tuzla, 34956, Istanbul, Turkey



ARTICLE INFO

Keywords:

Photo-supercapacitor
Graphene oxide
Zinc oxide
Solar energy storage

ABSTRACT

The development of photo-supercapacitors (PSC), which is an important step towards more efficient use of solar energy and reducing the carbon footprint, will be possible with a better understanding and manipulation of the properties of photo-active dual-effect electrodes used in these devices. This work demonstrates the existence of critical ratios for graphene oxide/zinc oxide (GO/ZnO) composites in terms of PSC performance. In this ratio, both photoluminescence intensity in the UV region and the defect densities determined from electron paramagnetic resonance spectroscopy are low. Moreover, the specific capacitance of the best-performing GO/ZnO composites increased 2.7-fold and reached 6612 mFg⁻¹ after UV illumination. Besides, this device showed exceptional stability over 30,000 galvanostatic charge and discharge cycles with 99.6 % capacitance retention and 100 % Coulombic efficiency. The maximum energy density of 6.3 Whkg⁻¹ and power density of 625 Wkg⁻¹ were calculated for a 2.5 V operating voltage under UV illumination. As proof of concept, a digital watch was powered for more than 1 h and 40 min with GO/ZnO-based PSC charging under UV and AM1.5 sunlight illumination at 0.2 Ag⁻¹ for 50 and 130 s, respectively.

1. Introduction

Among all other renewable energy sources, solar energy stands out with its great potential. Solar energy conversion systems can produce all the energy we need globally if used efficiently. Tremendous efforts have been paid for innovative, cost-effective production methods, materials, and storage technologies to use solar energy more effectively [1–7]. On the other hand, like other renewable energy sources, solar energy should be stored to use on demand. There are many different routes to store solar energy, including photo-electrochemical redox batteries, solar hydrogen generation, and solar fuel generation via carbon dioxide reduction [7–12]. Compared to these technologies, photo-supercapacitors (PSC) are the most attractive technology as they enable solar energy storage by directly converting it into electricity

[13–23]. The design of PSC devices should be simple and cost-effective to ensure effective use. However, designs with separately integrated solar cells are moving away from this direction. In recent years, in innovative designs, including our works, solar energy can be absorbed and stored on the same electrode employing dual-use photo-active electrodes [24–30]. Thus, a new generation of energy conversion-storage devices, which are as simple as the design of supercapacitors and increase their performance under light, are being developed.

As in supercapacitor applications, increasing energy density is one of the most important issues in PSC devices. In addition, the structure of the photo-active electrode, which provides the absorption of solar energy, is not complex in a way that keeps the cost as low as possible. Therefore, we focused on increasing the specific capacitance (C_p), energy density (E_d), and cycle stability of ZnO-based PSC devices

* Corresponding authors at: Department of Materials Science and Nanotechnology Engineering, TOBB University of Economics and Technology, Sogutozu Caddesi No 43 Sogutozu, 06560 Ankara, Turkey.

E-mail addresses: msankir@etu.edu.tr (M. Sankir), nsankir@etu.edu.tr (N.D. Sankir).

<https://doi.org/10.1016/j.est.2023.107694>

Received 2 February 2023; Received in revised form 14 April 2023; Accepted 10 May 2023

Available online 18 May 2023

2352-152X/© 2023 Elsevier Ltd. All rights reserved.

[15,24,25]. In a general manner, the two most important key components of PSC devices are the active electrode properties and separators. In this respect, dual-functionalized electrodes must have good light absorption properties so that they provide the formation of light-generated electron-hole pairs. These light-generated electrons and holes increase the charge amount stored on the electrodes. Thus, using grid electricity from fossil fuel sources will be reduced and ultimately zeroed.

Graphene oxide (GO) and zinc oxide (ZnO) composite structures provide both the advantages of 2D materials, such as large surface area and superior electrical properties, as well as the advantages of ZnO, such as high UV absorption and catalytic activity. Therefore, they have come to the fore in different applications, from electrochemical sensor applications to antibacterial activity [31–34]. GO/ZnO-based composites have also been used in the supercapacitor field [35–38]. These composites not only provide enhancement in the specific capacitance but also extend the device's stability. Previously, our group reported the GO/ZnO nanowire composite electrodes for PSCs [24]. In that work, we have compared the performance of GO and rGO ZnO nanowire-based composites integrated into PSC as a photo-active electrode. It has been proved that GO/ZnO composites are superior to rGO/ZnO composites, especially in terms of stability, due to the presence of carbonaceous-based defects and the larger number of carbon layers [24].

In this study, we prepared GO/ZnO nanocomposites in different weight ratios and focused on composites' morphological, structural, and optical properties with the PSC performance results. In addition, the effects of varying ZnO amounts on the defect density were investigated by electron paramagnetic resonance spectroscopy (EPR) to establish a more in-depth connection between material properties and performance. It is known that the vacancy and interstitial defects seen in ZnO nanostructures change the optical, photo-electrochemical, and catalytic properties of the materials [12,39,40]. Although ZnO's defective nature and properties have been studied extensively, the composites of ZnO with 2D material are still subject to interest [41–45]. Previously X. Pan et al. reported that the introduction of GO could create oxygen vacancies in the lattice of ZnO crystals resulting in visible light photoactivity [44]. Recently, B. Saini et al. reported that the photocatalytic activity of the Ti_3C_2 MXene increased via ZnO doping, which introduced the oxygen vacancy in the composite [45]. In terms of the photocatalytic activity of ZnO, it is known that defect states lower the fast recombination of electrons and holes, therefore increasing charge transport and accelerating the activity [46]. It has also been reported that oxygen defects in metal oxides affect the performance of energy conversion and storage devices [47]. Previously, hydrogenated titanium dioxide (TiO_2) and zinc oxide (ZnO)-based electrodes have been integrated into supercapacitors [48–51]. It is known that hydrogenation creates oxygen vacancy in TiO_2 and ZnO, allowing the oxidation/ reduction of surface hydroxyl groups, which enhances the pseudocapacitive characteristic. However, it is important to emphasize that electrodes were tested in aqueous solutions in all these works. The effect of the surface defects differs from solid-state to aqueous systems.

In this study, we changed the defect structures in the composite by changing the GO:ZnO ratio. In other words, we manipulated oxygen defects, which are thought to have an effect, especially in electrochemical conversion and storage devices. With this study, we have taken an important step towards more widespread use of dual-effect devices that both convert and store solar energy in the future, explaining how the material properties of different composites affect the performance of solid-state PSC devices.

2. Experimental section

2.1. Materials

Zinc nitrate hexahydrate ($\text{Zn}(\text{NO}_3)_2 \cdot 6\text{H}_2\text{O}$, Sigma Aldrich, 98 % reagent grade) and ammonium hydroxide (NH_4OH , Sigma Aldrich, 38 %

have been used for the ZnO synthesis. Lithium chloride (LiCl, Emsure, ACS, Reagent) and polyvinyl alcohol (PVA, Merck) were used to prepare gel electrolytes.

2.2. Synthesis of photoactive composite materials

GO and ZnO nanowires (ZnO NW) have been synthesized as described in our previous work [24]. GO was prepared from graphite powder following the next steps: preoxidation, oxidation by an original modified Hummers method, exfoliation by sonication, and drying by lyophilization. The composite photo-active material was synthesized by stirring GO and ZnO NW in 1:3, 1:5, and 1:8 wt% in 10 mL DMF solvent at 100 °C for 3 h. The resulting product was collected by centrifuge at 2000 rpm for 5 min, after which it was vacuum-dried at 80 °C for 8 h.

2.3. Characterization

Raman Spectroscopy measurements were performed in a Renishaw Raman InVia System using a laser excitation wavelength of 532 nm green laser with a 50× objective at room temperature. UV-VIS. A HeCd laser (325 nm) was employed for the photoluminescence (PL) measurements, and the emission spectra were recorded in the 350–1100 nm range with an Ocean Optics Spectrometer QE65. Environmental scanning electron microscopy (ESEM) images were collected on a QUANTA 400F Field Emission SEM. The morphology and structural properties of the ZnO-GO nanostructures were investigated by transmission electron microscopy (TEM) (JEOL ARM 200F) with a high-resolution transmission electron microscope (200 kV) equipped with an EDX analyzer. Electron paramagnetic resonance (EPR) spectroscopy measurements, both in X and Q-band, were carried out on a dual-band E500 ELESYS (Bruker) spectrometer, combined with an M365FP1 UV-diode (Thorlabs), which was used for irradiation ($\lambda = 365$ nm with a power of 9.8 mW).

2.4. Photoelectrode preparation and electrochemical measurements

The FTO substrates were cleaned sequentially by sonication in alconox, deionized (DI) water, acetone, and ethanol. The colloidal solution of the synthesized composite material was prepared in an alcohol mixture (isopropanol/methanol/butanol) by sonication for 30 min and drop cast on the pre-cleaned FTO (loaded mass 10 mg). The PSC device assembly, PVA-LiCl electrolyte, was applied as the gel electrolyte. LiCl-PVA gel electrolyte was prepared as described in our previous work [24]. The active photoelectrode, a piece of filter paper, carbon paper, and bare FTO-coated glass as a counter electrode were wetted with the gel electrode, and device assembly was performed. The PSC devices' galvanostatic charge-discharge (GCD) and Cyclic voltammetry (CV) analysis were performed using a Gamry electrochemical workstation. A UV light source (FEMTO-TERA, 8.8 $\text{mW} \cdot \text{cm}^{-2}$) was used for illuminated environment-dependent electrochemical measurements. The basic supercapacitor parameters, such as specific capacitance (C_p), energy density (E_d), power density (P_d), and Coulombic Efficiency (CE%), were evaluated as reported in our previous studies [24,25]. Detailed equations are given in the Supplementary file.

3. Results and discussion

3.1. Materials characterization

The surface morphology of the GO/ZnO-based composites investigated via SEM can be seen in Fig. 1(a). GO flakes distributed quite well between ZnO nanorods in all three used ratios are observable. In addition, it is noteworthy that with the decrease of the ZnO amount, especially at the ratio of 1:3, a more clustered structure is formed. SEM images at different magnifications can be seen in Fig. S1 in the Supporting Info (SI) file. The Raman spectra of the three different GO:ZnO

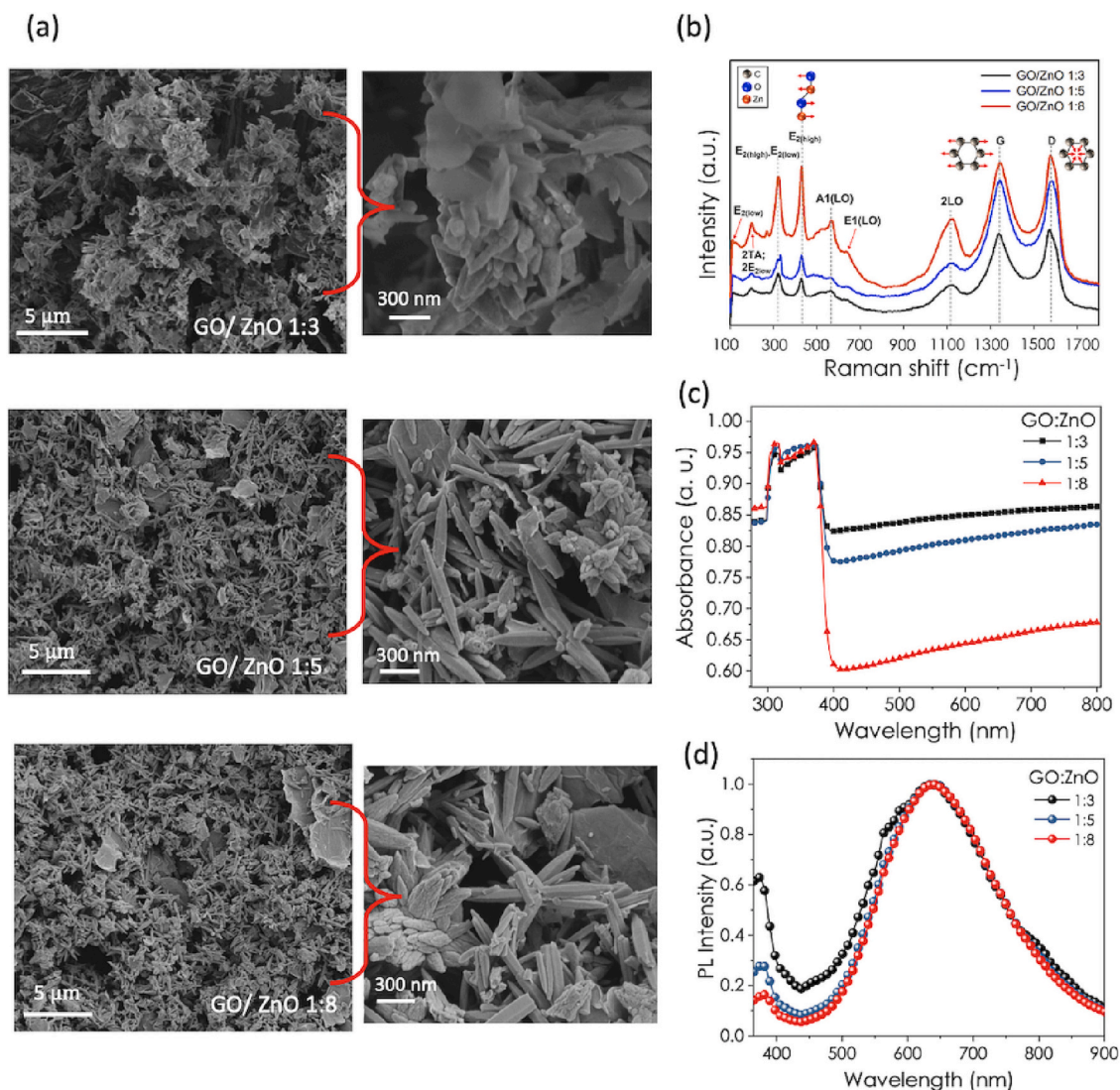


Fig. 1. (a) SEM images, (b) First-order and second-order Raman spectra, (c) UV-Vis spectroscopy, (d) PL spectroscopy of GO:ZnO nanocomposites.

nanostructures are given in Fig. 1(b), revealing the differences as a function of different GO:ZnO weight ratios. Due to the predominance of E2 modes in standard backscattering experiments, these modes can be used as a Raman fingerprint for ZnO [52]. Fig. 1(b) shows a sharp peak at about 428 cm⁻¹ assigned to characteristic Wurtzite E_{2(high)} mode for ZnO. This peak is shifted to lower wavelengths in the case of higher GO concentrations, which may be due to possible spatial variances in the strain that cause an anisotropic response of ZnO.

Another strong vibration at 321 cm⁻¹ is generally attributed to the second-order Raman process and assigned to the E_{2(high)}-E_{2(low)} difference mode, which was confirmed by both symmetry considerations and temperature-dependent intensity analysis [52–54]. The relatively weak and broad bands detected in the spectra at about 565 cm⁻¹ can be assigned to the A₁(LO) phonon mode, which occurs when the c-axis of wurtzite ZnO is parallel to the sample surface. Looking at the high-frequency range, one can deduce that the most significant second-order features correspond to LO overtones and the combinations of LO modes. The broad bands between 1030 and 1200 cm⁻¹ likely belong to the multiphoton process, and the wide peak at around 1120 cm⁻¹ may correspond to 2LO scattering from flat bands along the A-L-M line, possibly in combination with the modes 2A₁ (LO) and 2E₁ (LO) at the Γ symmetry point of the Brillouin zone. As for the GO occurrence in the structure, the peaks around 1340 cm⁻¹ and 1570 cm⁻¹ indicate the G

and 2D bands, respectively [24,54]. The D band is due to the transverse optical phonons around the K corner of the first Brillouin zone, originating from the breathing modes of the six-atom rings of graphene [55]. Activation of such a mode is connected with a defect in the structure. On the other hand, the G band emanates from a first-order Raman scattering by in-plane optical transverse and longitudinal phonons at the Brillouin zone center [54,55]. Room temperature frequencies and symmetries of the first- and second-order Raman spectra observed in different ZnO:GO molar ratios are listed in Table S1. UV-Vis spectra of GO/ZnO composites are presented in Fig. 1(c). It was observed that the optical absorption between 400 and 800 nm increased with the amount of GO in the composites. Since more electron-hole pairs are created by optical absorption, an increase in the GO content in the structure means that more charge carriers will be created. Fig. 1(d) shows the normalized PL spectra of ZnO modified by GO and excited with a 325 nm laser. The PL spectra show two emission bands at 640 (1.94 eV) and 375 nm (3.24 eV), respectively, where the broad and intense peak in the visible range corresponds to deep-level emission [56–58]. The PL peak centered in the UV range relates to the near-band exciton emission [57]. The modification by GO of ZnO does not change the shape of the PL curve. One may observe the decrease of the UV peak by changing the ratio from 1:3 to 1:8. Besides, the UV peak position is shifted from 374 nm (1:3 sample) to 380 nm (1:8 sample), which could be explained by the GO sheets

anchored to the ZnO surface.

TEM images of ZnO modified by GO with different concentrations are presented in Fig. 2. Fig. 2(a)–(c) shows the average diameter and the length of the used ZnO nanowires around 100 ± 20 nm and 900 ± 200 nm, respectively. All samples indicate the presence of GO sheets with different lateral sizes. As observed in the SEM measurements, the ZnO nanowires are overlapped with GO flakes enabling electron conduction pathways through the GO sheets. Moreover, the EDX mapping images for GO/ZnO (1:3) are given in Fig. 2(d). Fig. 2(e) exhibits the XRD spectra of the composite materials. The Bragg diffraction peaks from ZnO nanowire were observed at 31.6° , 34.4° , 36.3° , 47.5° , 56.5° , 62.5° and 68.1° indexed to (100), (002), (101), (102), (110), (103) and (112) at different diffraction angles, respectively [59]. The characteristic signal observed at 10.2° belonging to the GO (001) diffraction angle gradually disappears when the ZnO ratio increases.

The surface element composition and chemical state were investigated via XPS spectroscopy. Fig. 2(f) shows the XPS survey spectrum of GO/ZnO (1:5) indicating the presence of C, Zn, and O as the main

elements. The high-resolution XPS spectrum of Zn (Fig. 2(g)) shows that two typical Zn 2p peaks appear at 1021.7 and 1044.7 eV which correspond to Zn 2p_{3/2} and Zn 2p_{1/2}, respectively. The spin–orbit splitting is almost identical with the pristine ZnO (~ 23.0 eV) confirming that there is no covalent bonding between GO and ZnO [59]. The C 1s spectrum (Fig. 2(h)) of GO/ZnO can be deconvoluted into three Gaussian peaks where the signals originate from (i) the C–C or C=C bond at 283.7 eV, (ii) C–O bond from alkoxy group at 284.7, and (iii) carboxyl O–C=O bond at 287.6 eV [60]. The O 1s spectrum can be deconvoluted into two Gaussian peaks at 529.1 and 531.0 eV (Fig. 2(i)). These two Gaussian peaks can be assigned to the ZnO's lattice oxygen and the oxygen in C–OH/C–O–C of the GO/ZnO, respectively.

EPR spectroscopy was employed to analyze the defect centers present in the composite materials. Fig. 3(a) depicts the X-band EPR spectra of the GO/ZnO-based composites, showing an intense signal with a g-value of 2.0034, which is characteristic of carbon-related defects in the GO material (inset of Fig. 3a) [24], which suggests that unpaired electrons, hence electron spins, are carbon-based although located on the

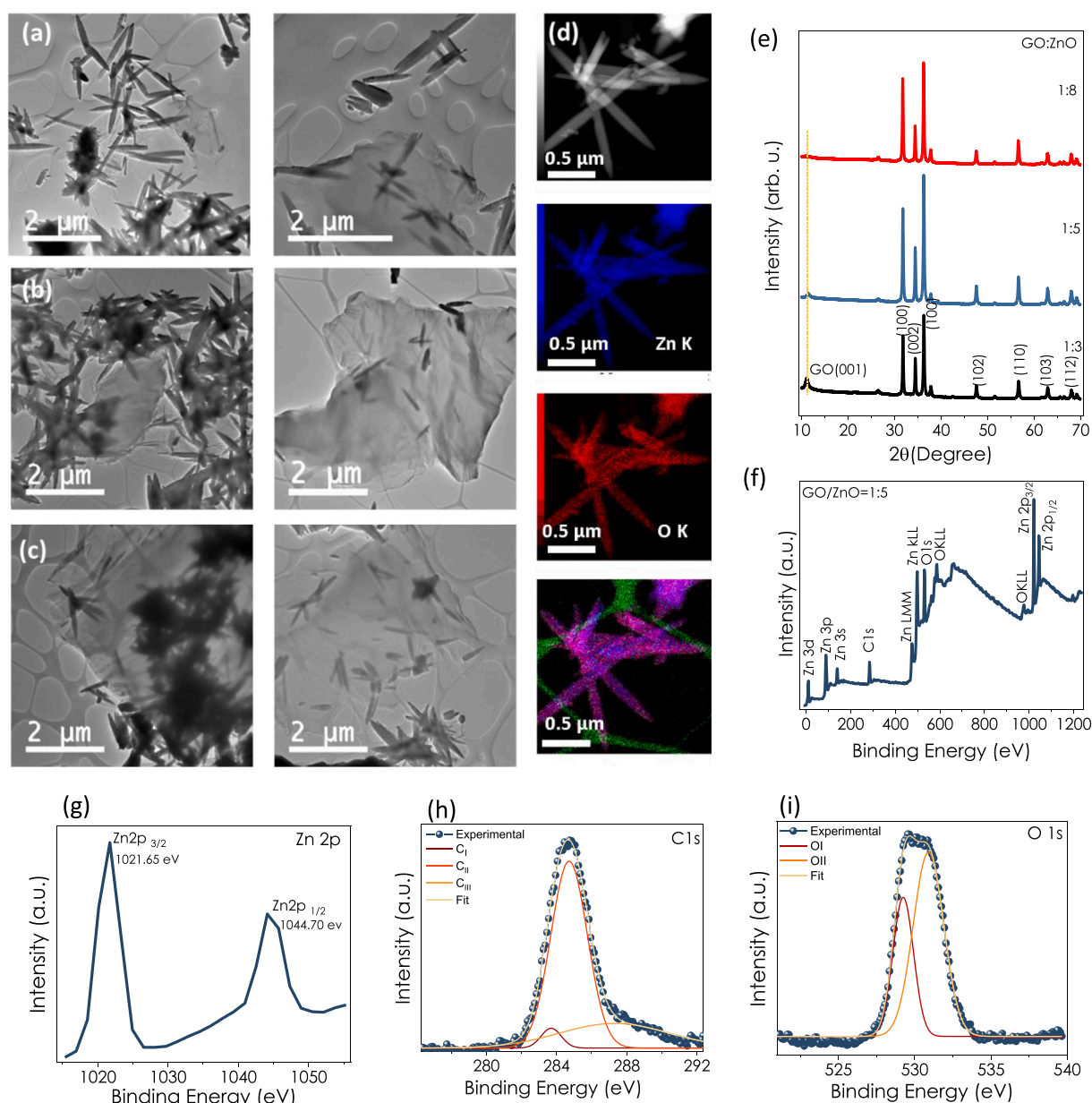


Fig. 2. TEM images of GO/ZnO with 1:3 (a), 1:5 (b), and 1:8 (c) ratios; (d) EDX mapping of ZnO nanowires in GO/ZnO with a 1:3 ratio, (e) XRD patterns of GO/ZnO nanocomposites, (f) XPS survey, high-resolution XPS spectra for (g) Zn 2p, (h) C 1s, (i) O 1s.

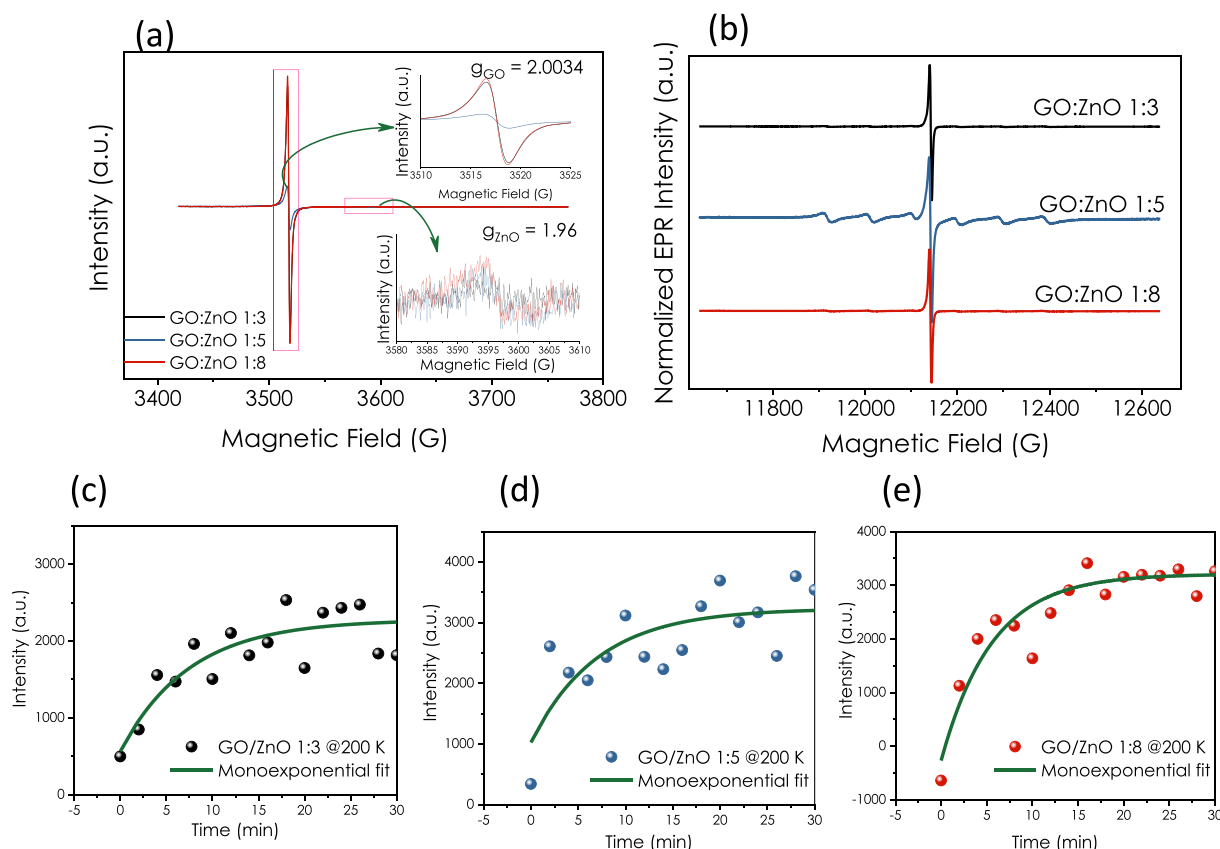


Fig. 3. EPR spectra of the GO/ZnO-based composites (1:3, 1:5, and 1:8 ratios) in (a) X- and (b) Q-band. Evolution of the ZnO-related core defect EPR signal intensity ($g_{\text{ZnO}} = 1.96$) under UV irradiation, EPR spectra measured at 200 K for (c) 1:3, (d) 1:5, (e) 1:8 ratios.

carbon atoms in proximity to oxygen atoms. Compared to the EPR signal, a very weak ZnO-related EPR signal is observable, characterized by a 1.96 g-value (inset of Fig. 3a). Since the same amount of sample was used for the EPR measurements, a direct comparison between the EPR signal intensities is possible, showing that the composite with the 1:5 ratio has a very low carbon-related defect concentration compared to the other tested ratios, 1:3 and 1:8.

Q-band EPR measurements (Fig. 3(b)) revealed that the GO EPR resonance signal is superimposed to an impurity-type wide six-line EPR signal characteristic for Mn^{2+} , originating from KMnO_4 used in the synthesis procedure of the GO material. As reported in a previous study [24], in GO/ZnO-based composites irradiated with UV light at room temperature, no evolution of the ZnO-related core defect is observable because of a fast charge transfer; this process is significantly slowed down at lower temperatures. Hence the EPR signal intensity of the ZnO core defects was monitored over 30 min under UV irradiation. The results are presented in Fig. 3(c)–(e), from which, after a monoexponential fit, the photogenerated ZnO core defect's reaction constants were obtained with $k_{1:3} = 0.133 \text{ min}^{-1}$, $k_{1:5} = 0.142 \text{ min}^{-1}$, $k_{1:8} = 0.222 \text{ min}^{-1}$. In addition, the stability of the pristine GO and GO/ZnO (1:5) composite films was determined by FTIR and UV–Vis spectroscopy upon applying continuous UV irradiation for 15 min intervals (Fig. S2). The FTIR spectra of pristine GO thin film showed an absorption peak at 1617 cm^{-1} due to the $\text{C}=\text{C}$ stretching mode and the peaks at 1718, 1165, and 1033 cm^{-1} , corresponding to the stretching modes of $\text{C}=\text{O}$, $\text{C}-\text{OH}$, and $\text{C}-\text{O}$, respectively. The transformation of GO to reduced GO (rGO) can be detected from the $\text{C}-\text{O}$ and $\text{C}=\text{O}$ stretching modes in the FTIR spectrum [61]. The preservation of the characteristic peaks at 1033 and 1718 cm^{-1} for $\text{C}-\text{O}$ and $\text{C}=\text{O}$ stretching modes, respectively, indicated that there was no reduction of GO to rGO upon UV exposure.

3.2. Photo-electrochemical characterization of the solid-state PSC devices

Cyclic voltammetry (CV) measurements of the GO/ZnO composites having ratios of 1:3, 1:5, and 1:8 have been performed in dark and UV illumination conditions. Fig. 4 (a) and (b) show the CV measured at a 200 mVs^{-1} scan rate under dark and UV-radiation, respectively. The specific capacitance (C_p) values, calculated from the CV curves, are given in Fig. 4 (c). At a 10 mVs^{-1} scan rate, the most significant increase with UV illumination has been observed for the 1:5 ratio. In other words, the C_p of 2427 mFg^{-1} increased 2.7-fold and reached 6612 mFg^{-1} after UV-illumination. The CV measurements at various scan rates for PSC devices prepared with 1:3 and 1:8 ratios are given in Fig. S3. The performance increase of the GO/ZnO composite with a 1:5 ratio has also come to the fore in open circuit potential (V_{oc}) measurements. Fig. 4(d) shows that the maximum V_{oc} of 0.6 V has been observed for the PSC with GO/ZnO 1:5 as a photo-active electrode. The charge relation time of this device after turning off the UV light was also superior to the other ratios. The most important reason for this sensitivity to UV illumination, and therefore, the increase in performance is thought to be the difference in the defect structures summarized in the EPR measurements.

Results of the galvanostatic charge-discharge (GCD) analysis have been summarized in Fig. 4(e)–(g) and Fig. S4. At 0.05 Ag^{-1} current density and 1.5 V, operating potential, C_p and energy density (E_d) of GO/ZnO 1:5 were 2866 mFg^{-1} and 3224 mJkg^{-1} , respectively, under UV illumination. Other GO/ZnO ratios resulted in lower C_p and E_d than the 1:5 ratio, indicating an optimum GO:ZnO ratio in the composite in terms of structural, morphological, and electrochemical properties. Previously our research group reported that the GO/ZnO 1:10 ratio resulted in the maximum C_p and E_d of 2200 mFg^{-1} and 2469 mJkg^{-1} , respectively [24]. As a result, with this study, we could go one step further in producing GO/ZnO composite electrodes for PSC devices, which we pioneered. In

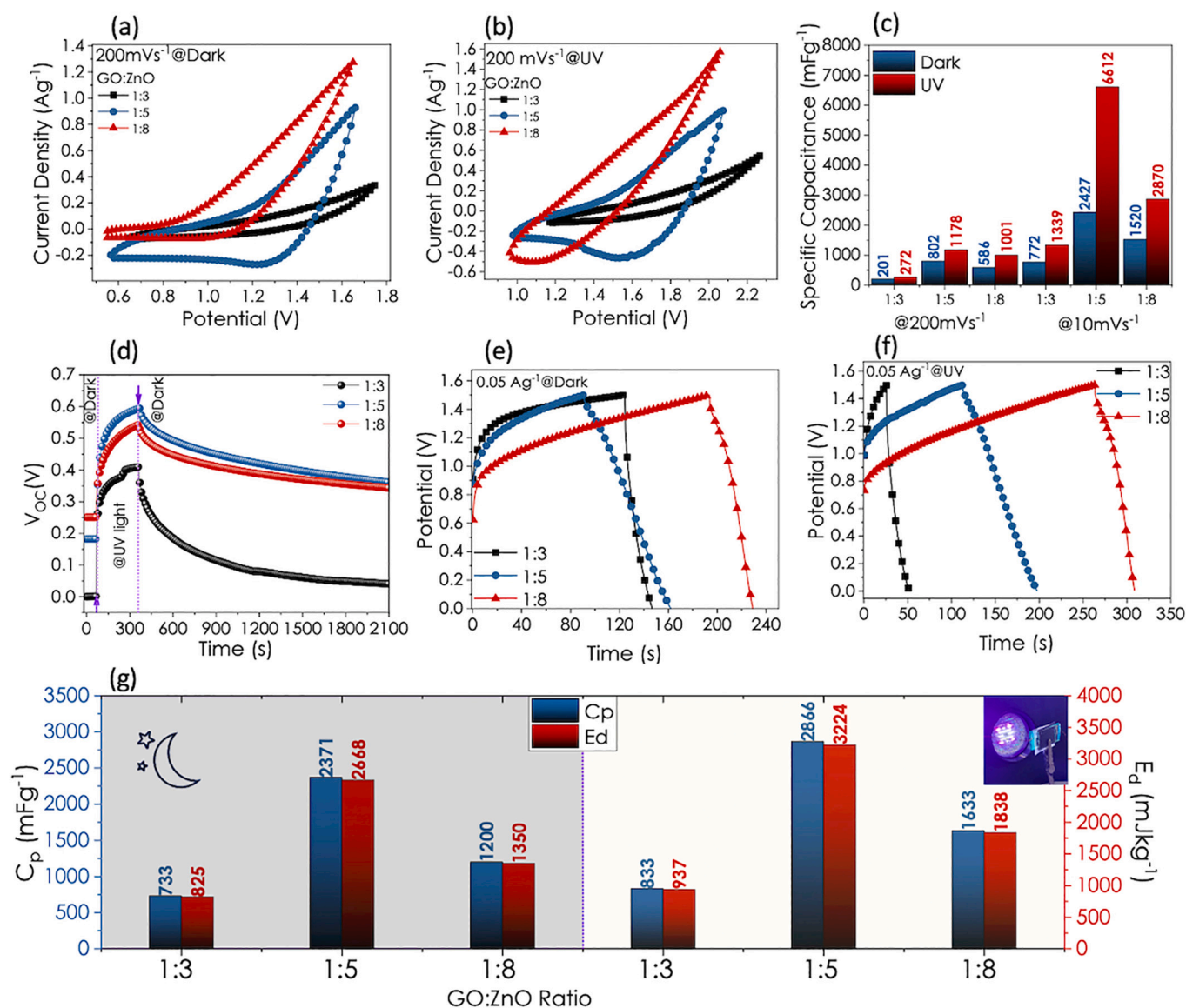


Fig. 4. Comparison of the CV scans of GO:ZnO (1:3, 1:5, and 1:8) based PSC device (a) in the dark and (b) under UV radiation at a 200 mVs⁻¹ scan rate, (c) Comparison of Cp values obtained from CV scans at 10 and 200 mVs⁻¹ scan rates, (d) the relative change in Voc of PSC devices upon UV on-off conditions, Comparison of the GCD curves obtained at a 0.05 Ag⁻¹ current density (e) in the dark and, (f) under UV radiation, (g) Calculated Cp and Ed values of the PSC devices at dark and under UV radiation.

light of the photo-electrochemical analyses, it can be concluded that there is an optimum ratio between the components for the GO/ZnO composites we prepared. As the amount of ZnO in the composite increased, the energy density as a result of UV illumination compared to the dark values also increased. When we look at the Ed(@UV)/Ed(@dark) ratios in the 1:3, 1:5, and 1:8 samples, the calculated values were 1.14, 1.21, and 1.36, respectively. However, when we analyze it in terms of value, the Ed value of the 1:5 sample under UV illumination is higher than for the other ratios. As a result, while having more ZnO in the structure increases the light sensitivity, GO provides more charge storage.

Further electrochemical analysis has been performed via impedance spectroscopy. The EIS analysis results of the composite PSC devices in the frequency range of 100 mHz to 100 kHz collected in the dark and under UV irradiation have been displayed in Fig. 5. The Nyquist plots of each PSC device exhibit a small semi-circle in the high-frequency region. The Nyquist plots have been fitted well with the EC Lab program to give the same equivalent electrical circuit (EC) model for all PSC devices in the dark and under UV radiation (Fig. 5(a), inset). The detailed EC

parameters are listed in Table S2. In the suggested EC, the electrode's ohmic resistance is denoted as R1, while R2 and R3 signify the charge transfer resistance. On the other hand, Q is the constant phase element, representing the double-layer capacitance. Here, the element representing the Warburg impedance is present because of the semi-straight part in the EIS spectra in the lowest-frequency region, showing that the electrochemical process is associated with the diffusion-controlled manner of the composite materials. As the UV light is on, the R1 value remains unchanged. At the same time, the charge transfer resistance drops enormously for all PSC devices, indicating much more efficient charge transfer throughout the electrodes. Bode plots of the PSC devices obtained from the 1:5 ratio and other ratios in the dark and under UV radiation have been given in Figs. 5(c)-(d) and Fig. S5, respectively. The characteristic frequency at which the phase angle reaches -45° is defined as the characteristic frequency (f0). The relaxation time constants (τ0) can be found from the reciprocal of the characteristic frequency. At this point the capacitive and the resistive impedances become equal and after this point, the supercapacitors show more resistive behavior at higher frequencies. The corresponding relaxation

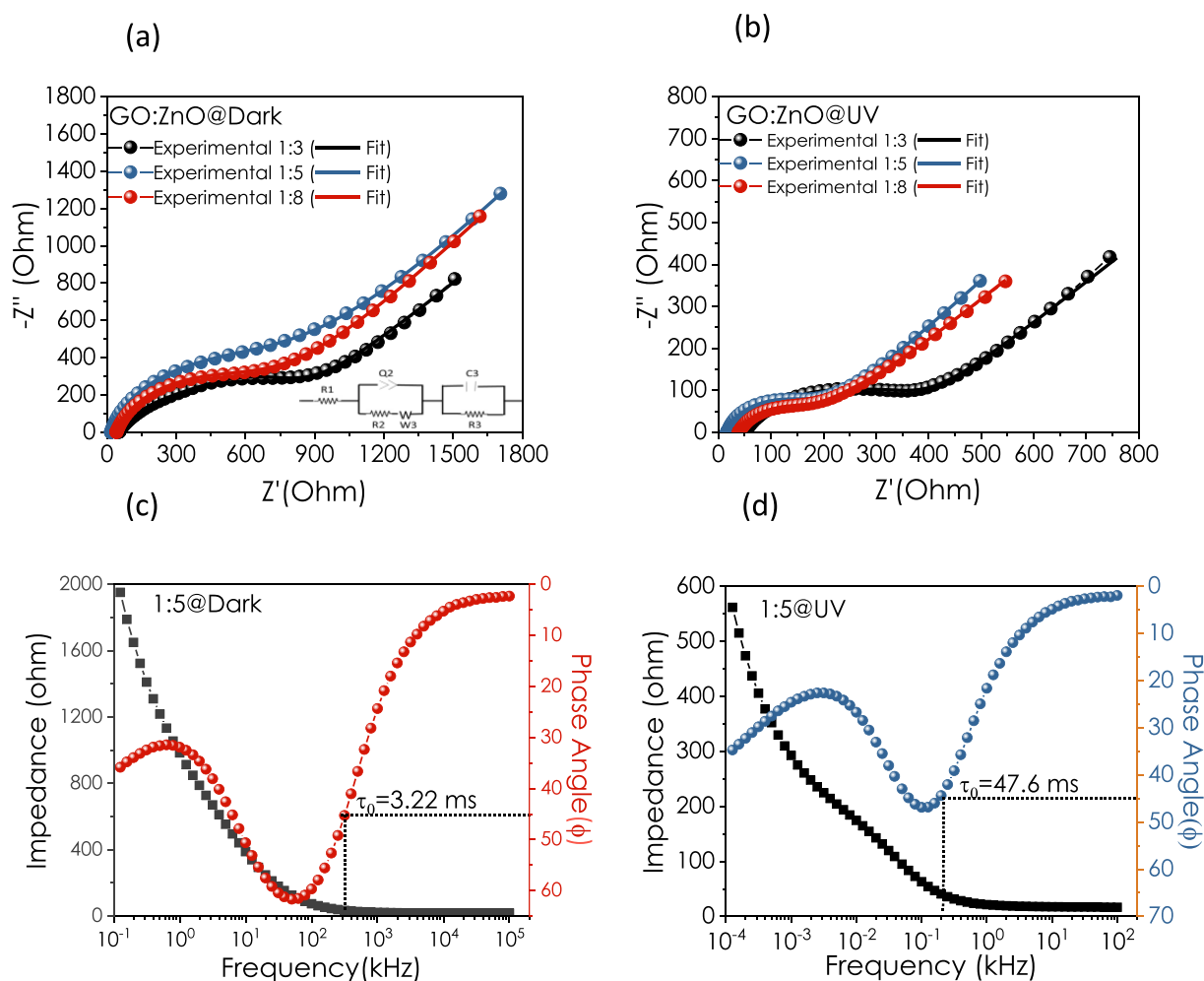


Fig. 5. EIS analysis results: Nyquist plots of all PSC devices (a) in the dark, and (b) under UV radiation, Bode plots (c) in the dark, and (d) under UV irradiation of the PSC (1:5) device.

time constant (τ_0) is the minimum time needed to discharge all the energy from the device with an efficiency greater than 50 % [62]. In other words, lower τ_0 under dark conditions implies the capability of fast discharge resulting from high-speed ion diffusion and transport behavior. Since the PSC device with GO: ZnO = 1:5 ratio is more efficient than the other studied ratios, we delved into the performance analysis of this PSC device. Figs. 6(a) and (b) display the CV scan curves taken at various scan rates under dark and UV illumination, respectively. It is observed that the higher CV area has been obtained under UV radiation, and the maximum enhancement in Cp value has been seen at a 10 mVs^{-1} scan rate as increasing from 2.43 to 6.61 Fg^{-1} (Fig. 6(c)).

Besides increasing CV capacitance, a distinguished shift to positive potential has been observed, due to the higher open circuit potential under UV radiation. Further, the GCD curves collected at various current densities under UV radiation have been given in Figs. 6(d) and (e), respectively. At a low current density (0.05 Ag^{-1}), the Cp value increased from 2.33 to 2.87 Fg^{-1} , from dark to UV-on condition. On the other hand, the E_d value has increased from 2.62 to 3.63 Jkg^{-1} under UV radiation. Moreover, Coulombic Efficiency (CE%) values have been calculated for PSC (1:5) from the GCD analysis collected at 1 V under UV light at dark (Fig. 6f). At low current densities, it was observed that the CE% value exceeds %100, possibly owing to the additional electron-hole pair generation and thus, enhanced electron transfer between electrodes under UV irradiation. Fig. S6 displays the GCD curves at different potentials in the dark, under UV and AM 1.5 solar light irradiation at various operating potentials such as 1 V, 2 V, and 2.5 V. The prolonged

discharge time resulted in the PSC's Cp value which reached 6.90 Fg^{-1} under UV irradiation, while this value was 2.75 Fg^{-1} (at 0.03 Ag^{-1} current density).

In Fig. 6(f), the long-term GCD data, collected at 0.12 Ag^{-1} of current density, display the excellent stability of the fabricated PSC device with 99.6 % of Cp retention value and 100 % of Coulombic Efficiency after 30,000 successive cycles. The stability of the PSC device was confirmed with the CV and GCD analysis obtained before and after 10,000 cycles with aging over 6 months in the air at a 10 mVs^{-1} scan rate and a 0.12 Ag^{-1} of current density, respectively (Fig. S7). Table 1 summarizes the recent photo supercapacitor devices' detailed performance and important device parameters, including the present results. This table shows that our device provides one of the highest performances with excellent stability, up to 30,000 cycles. Fig. 7(a) displays the photo-charging process under an applied current density of 0.2 Ag^{-1} and a photographic image of the PSC device during photo charging. The Inset of Fig. 7(a) shows the self-discharge of the PSC device in the dark under an open circuit potential. As seen in this inset figure total discharge of the device has not been achieved for more than 10,000 s. In other words, the V_{oc} of the device was around 0.6 V after 10,000 s indicating the high charge trapping of the GO/ZnO-based PSC. To demonstrate this performance a digital watch has been powered with the GO/ZnO (1:5)-based PSC (Fig. 7(b)). Before connecting the PSC to the digital watch, the device was charged under UV illumination at 0.2 Ag^{-1} for the 50s. Fig. 7(b) shows that, the digital watch worked for more than 1 h. This proof of concept showed that our device has a huge potential to be applied,

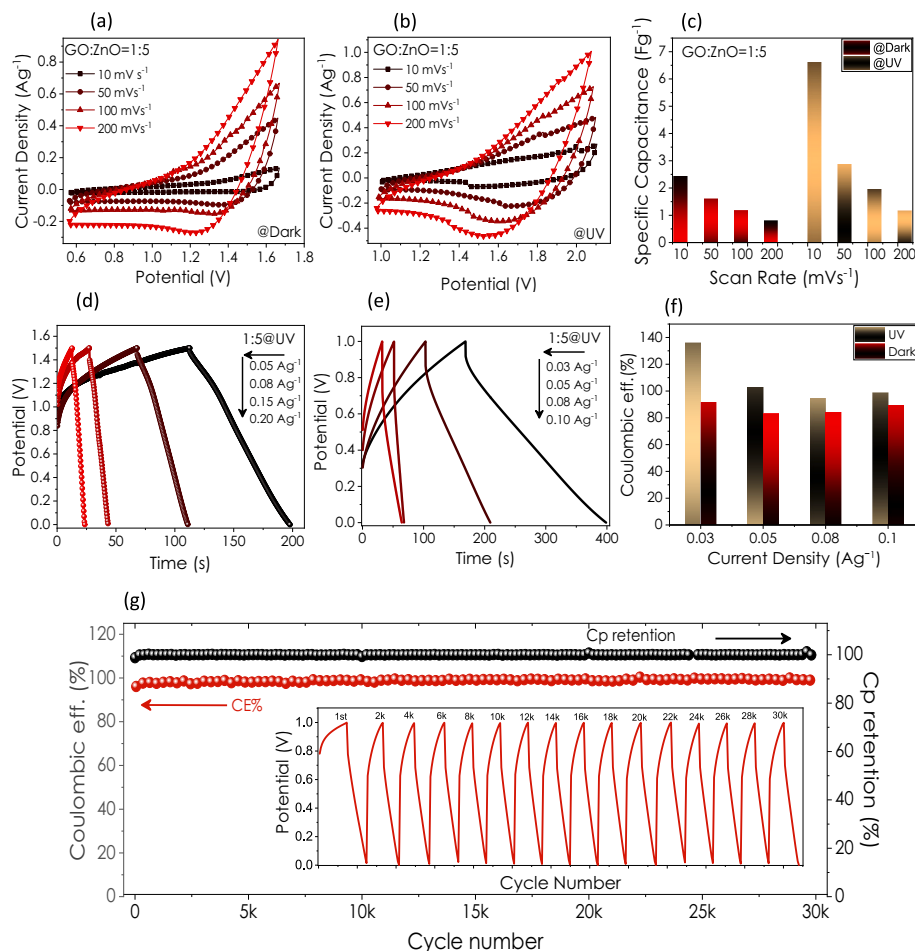


Fig. 6. Comparison of the CV of the PSC device (1:5) at various scan rates (a) in the dark, (b) under UV radiation, (c) Calculated C_p values at various scan rates, GCD curves at various current densities under UV radiation (d) at 1.5 V and (e) 1 V of operating potential, (f) Coulombic Efficiency values at 1 V of operating potential, (g) long-term stability (consecutive 30 k cycle) of the PCS device taken at 0.12 Ag^{-1} of current density, inset figure is the charging-discharging cycles taken at various cycle numbers.

Table 1
Literature comparison of photo supercapacitor devices.

PSC device	Electrolyte/separator	Operating potential	C_p	E_d	C_p retention (%)	Ref.
Perovskite/NC//NC	Silica gel electrolyte	1.2 V	33.8 mF cm^{-2}	$\sim 6.8 \text{ } \mu\text{Wh cm}^{-2}$	150@1000-cycle	[63]/2018
BiVO_4 -RGO	Na_2SO_4	0.3 V	$33.7 \text{ F g}^{-1} (@0.1 \text{ Ag}^{-1})$	NA	~ 75 @110-cycle	[64]/2020
N-MCN@GH	PVA/ H_2SO_4	1.0 V	$8.1 \text{ F cm}^{-3} (@1 \text{ A g}^{-1})$	$1.12 \text{ mW h cm}^{-3}$	80@10,000-cycle	[65]/2020
MnO_2 - V_2O_5 /WTiO ₂	1.0 M LiCl	0.5 V	$95 \text{ mF cm}^{-2} (@0.12 \text{ mA cm}^{-2})$	NA	94@5000 cycle	[29]/2022
Methylammonium bismuth triiodide (MBI)	Polymer gel electrolyte (PVA + CB + H_3PO_4)	1.0 V	$\sim 4.96 \text{ F g}^{-1}$ (CV scan @10mVs ⁻¹)	0.70 Wh kg^{-1}	94.79@5000-cycle (CV scan)	[66]/2022
V_2O_5 /ZnO	PVA-KCl/Filter paper	0.8 V	$20 \text{ mF g}^{-1} (@0.2 \text{ } \mu\text{Acm}^{-2})$	NA	175@5000-cycle	[67]/2023
PEDOT/ZnS/Ag ₂ S/ZnO	PVP/[HEMIIm][BF ₄]	0.4 V	$0.667 \text{ mF cm}^{-2} (@4 \text{ } \mu\text{Acm}^{-2})$	NA	100@1200-cycle	[68]/2020
g-C ₃ N ₄ /ZnO NW	PVA-LiCl/Nafion® 115	1.5 V	$0.46 \text{ F g}^{-1} (@53 \text{ mAg}^{-1})$	$0.45 \text{ Wh kg}^{-1} (@53 \text{ mAg}^{-1})$	90.2@25,000-cycle	[25]/2022
GO/ZnO NW	PVA-LiCl/Filter paper	1.5 V	$2.20 \text{ F g}^{-1} (@28 \text{ mAg}^{-1})$	$2.47 \text{ Wh kg}^{-1} (@28 \text{ mAg}^{-1})$	100@5000-cycle	[24]/2022
GO/ZnO NW	PVA-LiCl/Filter paper	2.5 V	$7.2 \text{ F g}^{-1} (@200 \text{ mAg}^{-1})$	$22.5 \text{ J kg}^{-1} (@200 \text{ mAg}^{-1})$	99.6@30,000-cycle	This work
		2.0 V	$2.81 \text{ F g}^{-1} (@200 \text{ mAg}^{-1})$	$5.62 \text{ J kg}^{-1} (@200 \text{ mAg}^{-1})$		
		1.5 V	$2.87 \text{ F g}^{-1} (@50 \text{ mAg}^{-1})$	$3.23 \text{ J kg}^{-1} (@50 \text{ mAg}^{-1})$		
		1.0 V	$6.90 \text{ F g}^{-1} (@30 \text{ mAg}^{-1})$	$3.45 \text{ J kg}^{-1} (@30 \text{ mAg}^{-1})$		

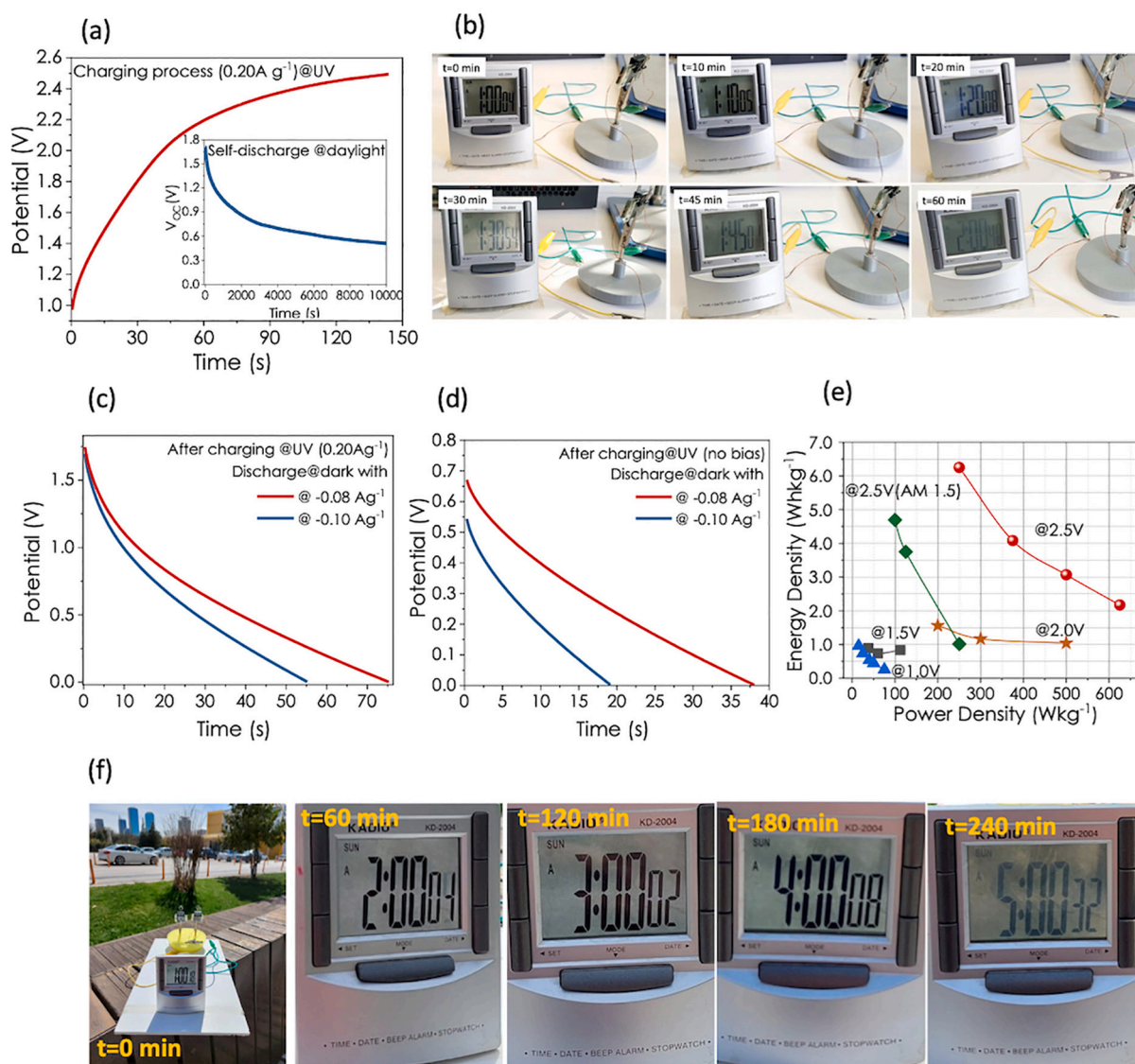


Fig. 7. (a) Photo-charging process of the PSC device under UV irradiation at a 0.2 A g⁻¹ current density, (b) Digital photos of the PSC device while connected to a watch, (c)-(d) discharge processes depending on various applied current densities after charging at 0.2 A g⁻¹ under UV irradiation, (e) Ragone plot illustrating the performance summary of the PSC device, (f) outdoor proof of concept experiment of 2cell-PSC charged at daylight and no-bias.

especially to portable devices. After applying 0.2 A g⁻¹ of current density under UV radiation, the discharging process at various current densities is given in Fig. 7c. On the other hand, Fig. 7d displays the discharge curves collected in dark conditions after the photo-charging process with no applied current. Finally, the Ragone plot in Fig. 7e summarizes the performance values of the GO-ZnO-based PSC device (1:5) under UV radiation and AM 1.5 sunlight simulation. Expectedly, at higher potentials, the E_d and P_d values increased and have been calculated as 6.25 Whkg⁻¹ and 250 Wkg⁻¹ at a 2.5 V operating voltage under UV illumination, respectively. As shown in Fig. S6, GCD curves for various current densities have been obtained under AM 1.5 solar light, and maximum E_d and P_d have been calculated as 4.69 Whkg⁻¹ and P_d of 250 Wkg⁻¹, respectively. The outdoor proof-of-concept experiment is given in Fig. 7f, where after connecting two PSC cells in series, we kept them in daylight for a while (about 10s), and then it was observed that the clock worked for more than 4 h (Supplementary Video). Additionally, Fig. S8 displays the charging of PSC under sunlight (AM1.5) followed by connecting to a watch in dark conditions as the proof-of-concept experiments. It is seen that the GO/ZnO NW composite-based PSC devices we produced under the light of these results work more efficiently under UV

light, but also work in sunlight (under AM 1.5 condition) and perform quite well compared to the literature. Finally, the 2 PSC devices were connected in series for proof-of-concept experiments and related electrochemical analysis under UV light and dark conditions (Fig. S9). The V_{OC} analysis of the connected devices showed that the V_{OC} increased from 0.70 to 1.48 V when the UV light was turned on. Additionally, the charging time under UV light was shorter than that of dark conditions, while measured V_{OC} after charging at light retained a much longer time. Further outdoor experiments have been performed after charging 2cell-PSC at UV and 0.05 A g⁻¹ current density. In this case, the alarm watch was powered outdoors for about 5 h (Fig. S10). These studies carried out in daylight and outdoors showed better performance compared to the laboratory environment. This high performance proves that photo-generated charges can be retained for a long time in GO: ZnO-based PSCs (Fig. S11).

4. Conclusions

In this study, GO/ZnO composites with different weight ratios were prepared and utilized for PSC devices using PVA/LiCl, filter paper, and

carbon paper as gel electrolytes, separators, and conductive electrodes, respectively. Changing the GO:ZnO weight ratio while synthesizing the composite enhanced the optical absorption within the visible region. In addition, the PL intensity at the UV region increased with increasing the GO:ZnO ratio. EPR analysis revealed that the composite with the 1:5 ratio has a very low carbon-related defect concentration compared to the other tested ratios, 1:3 and 1:8. Moreover, the photogenerated ZnO defect's reaction constants were obtained with $k_{1:3} = 0.133 \text{ min}^{-1}$, $k_{1:5} = 0.142 \text{ min}^{-1}$, $k_{1:8} = 0.222 \text{ min}^{-1}$. The photo-electrochemical measurements revealed that the GO/ZnO composite having a 1:5 ratio was superior to other composites. Hence, the C_p calculated from the CV analysis at a 10 mVs^{-1} scan rate, increased 2.7-fold and reached 6612 mFg^{-1} after UV illumination. Moreover, GO/ZnO-based PSC was highly stable up to 30,000 cycles of GCD, having 99.6 and 100 %, capacitance retention and Coulombic Efficiency, respectively. The maximum C_p and E_d have been calculated as 7.2 Fg^{-1} and 22.5 Jkg^{-1} at a 2.5 V operating voltage under UV illumination, respectively. In conclusion, it has been determined that there is a critical ratio for GO/ZnO composites in terms of PSC performance. The defect density for this ratio is lower than for the other ratios, confirmed by PL and EPR analysis. In the future, we expect devices that provide both conversion and storage of solar energy to replace solar cells, especially in portable systems where lightness is at the forefront, with the creation of different heterojunctions or composite materials.

Supplementary data to this article can be found online at <https://doi.org/10.1016/j.est.2023.107694>.

CRediT authorship contribution statement

C.T.A. and T.O.C. performed the fabrication and characterization of samples. C.T.A. also contributed to the data analysis and preparation of the manuscript. A.M.R., I.D.Y., and E.E. performed the electron paramagnetic resonance measurements and data analysis. F.B. and E.E. performed the SEM and Raman analysis. M.M. and M.D.L. synthesized the graphene oxide powders. I. I. and E.C. performed the transmission electron microscopy analysis. I.I. also performed photoluminescence analysis. N.D.S. and M.S. are the primary investigators of the study. N.D.S. and M.S. performed the data analysis and wrote the manuscript. All authors reviewed and commented on the manuscript at all stages.

Declaration of competing interest

The authors declare that they have no known competing financial interests or personal relationships that could have appeared to influence the work reported in this paper.

Data availability

Data will be made available on request.

Acknowledgments

A.M.R., M.M. and M.D.L. acknowledge the partial financial support from the Romanian Ministry of Research, Innovation and Digitalization, Nucleu Program within the National Research Development and Innovation Plan 2022-2027, project number PN 23 24 01 01. E.E. and I.D.Y. acknowledge TUBITAK for financial support through the 2232-program (Grant No: 118C243). I.I. acknowledges the partial financial support from the National Science Centre of Poland from the SONATA BIS project 2020/38/E/ST5/00176.

References

- [1] S. Gressler, F. Part, S. Scherhauser, G. Obersteiner, M. Huber-Humer, Advanced materials for emerging photovoltaic systems – environmental hotspots in the production and end-of-life phase of organic, dye-sensitized, perovskite, and

- quantum dots solar cells, *Sustain. Mater. Technol.* 34 (2022), e00501, <https://doi.org/10.1016/j.susmat.2022.e00501>.
- [2] W. Zi, Z. Jin, S. Liu, B. Xu, Flexible perovskite solar cells based on green, continuous roll-to-roll printing technology, *J. Energy Chem.* 27 (2018) 971–989, <https://doi.org/10.1016/j.jechem.2018.01.027>.
- [3] N.D. Sankir, E. Aydin, E. Ugur, M. Sankir, Non-toxic and environmentally friendly route for preparation of copper indium sulfide based thin film solar cells, *J. Alloys Compd.* 640 (2015) 468–474, <https://doi.org/10.1016/j.jallcom.2015.04.013>.
- [4] F. Qiao, Y. Xie, Z. Weng, H. Chu, Ligand engineering of colloidal quantum dots and their application in all-inorganic tandem solar cells, *J. Energy Chem.* 50 (2020) 230–239, <https://doi.org/10.1016/j.jechem.2020.03.019>.
- [5] N.D. Sankir, E. Aydin, M. Sankir, A. Bozbey, Influence of excitation frequency on structural and electrical properties of spray pyrolyzed CuInS₂ thin films, *J. Mater. Process. Technol.* 214 (2014) 1879–1885, <https://doi.org/10.1016/j.jmatprotec.2014.04.005>.
- [6] C. Tuc Altaf, O. Coskun, A. Kumtepe, M. Sankir, N. Demirci Sankir, Bifunctional ZnO nanowire/ZnSnO₃ heterojunction thin films for photoelectrochemical water splitting and photodetector applications, *Mater. Lett.* 322 (2022), 132450, <https://doi.org/10.1016/j.matlet.2022.132450>.
- [7] A.A. İnada, S. Arman, B. Safaei, A novel review on the efficiency of nanomaterials for solar energy storage systems, *J. Energy Storage.* 55 (2022), 105661, <https://doi.org/10.1016/j.est.2022.105661>.
- [8] S. Liao, J. Shi, C. Ding, M. Liu, F. Xiong, N. Wang, J. Chen, C. Li, Photoelectrochemical regeneration of all vanadium redox species for construction of a solar rechargeable flow cell, *J. Energy Chem.* 27 (2018) 278–282, <https://doi.org/10.1016/j.jechem.2017.04.005>.
- [9] A. Kumtepe, C.T. Altaf, N.S. Sahsuvar, N. Abdullayeva, E. Koseoglu, M. Sankir, N. D. Sankir, Indium sulfide based photoelectrodes for all-vanadium photoelectrochemical redox flow batteries, *ACS Appl. Energy Mater.* 3 (2020) 3127–3133, <https://doi.org/10.1021/acsaem.9b02034>.
- [10] C.T. Altaf, N.S. Sahsuvar, N. Abdullayeva, O. Coskun, A. Kumtepe, E. Karagoz, M. Sankir, N. Demirci Sankir, Inverted configuration of Cu(In, Ga)S₂/In₂Sn₃Sn 3D-ZnO/ZnSnO₃Bilayer system for highly efficient photoelectrochemical water splitting, *ACS Sustain. Chem. Eng.* 8 (2020) 15209–15222, <https://doi.org/10.1021/acssuschemeng.0c04846>.
- [11] L. Zhou, R. Lv, Rational catalyst design and interface engineering for electrochemical CO₂ reduction to high-valued alcohols, *J. Energy Chem.* 70 (2022) 310–331, <https://doi.org/10.1016/j.jechem.2022.02.033>.
- [12] C.T. Altaf, N. Abdullayeva, O. Coskun, A. Kumtepe, I.D. Yildirim, E. Erdem, M. Liu, A. Bozbey, E. Agar, M. Sankir, N.D. Sankir, Efficiency enhancement in photoelectrochemical water splitting: defect passivation and boosted charge transfer kinetics of zinc oxide nanostructures via chalcopyrite/chalcogenide mix sensitization, *Phys. Rev. Mater.* 125403 (2021) 1–14, <https://doi.org/10.1103/PhysRevMaterials.5.125403>.
- [13] T. Miyasaka, T.N. Murakami, The photocapacitor: an efficient self-charging capacitor for direct storage of solar energy, *Appl. Phys. Lett.* 85 (2004) 3932–3934, <https://doi.org/10.1063/1.1810630>.
- [14] S.C. Lau, H.N. Lim, T.B.S.A. Ravoo, M.H. Yaacob, D.M. Grant, R.C.I. MacKenzie, I. Harrison, N.M. Huang, A three-electrode integrated photo-supercapacitor utilizing graphene-based intermediate bifunctional electrode, *Electrochim. Acta* 238 (2017) 178–184, <https://doi.org/10.1016/j.electacta.2017.04.003>.
- [15] C.T. Altaf, O. Coskun, A. Kumtepe, A.M. Rostas, I. Iatsunskiy, E. Coy, E. Erdem, M. Sankir, N.D. Sankir, Photo-supercapacitors based on nanoscaled ZnO, *Sci. Rep.* 12 (2022) 11487, <https://doi.org/10.1038/s41598-022-15180-z>.
- [16] G. Maheshwaran, P. Pandi, S. Suganya, B.A. Kumar, G. Ramalingam, M.R. Prabhu, S. Sudhahar, Fabrication of self charging supercapacitor based on two dimensional bismuthene-graphitic carbon nitride nanocomposite powered by dye sensitized solar cells, *J. Energy Storage* 56 (2022), 105900, <https://doi.org/10.1016/j.est.2022.105900>.
- [17] J. Yin, J. Li, L. Wang, B. Cai, X. Yang, X. Li, W. Lü, Integrated photoelectrochromic supercapacitor for applications in energy storage and smart windows, *J. Energy Storage* 51 (2022), 104460, <https://doi.org/10.1016/j.est.2022.104460>.
- [18] A. Das, S. Deshagani, R. Kumar, M. Deepa, Bifunctional photo-supercapacitor with a new architecture converts and stores solar energy as charge, *ACS Appl. Mater. Interfaces* 10 (2018) 35932–35945, <https://doi.org/10.1021/acsaami.8b11399>.
- [19] C.H. Ng, H.N. Lim, S. Hayase, Z. Zainal, S. Shafie, H.W. Lee, N.M. Huang, Cesium Lead halide inorganic-based perovskite-sensitized solar cell for photo-supercapacitor application under high humidity condition, *ACS Appl. Energy Mater.* 1 (2018) 692–699, <https://doi.org/10.1021/acsaem.7b00103>.
- [20] G. Maddala, M. Ambapuram, V. Tankasala, R. Mitty, Optimal dye sensitized solar cell and photocapacitor performance with efficient electrocatalytic SWCNH assisted carbon electrode, *ACS Appl. Energy Mater.* 4 (2021) 11225–11233, <https://doi.org/10.1021/acsaem.1c02087>.
- [21] X.L. Li, K.C. Long, G. Zhang, W.T. Zou, S.Q. Jiang, D.Y. Zhang, J.Q. Zhou, M.J. Liu, G.J. Yang, Lead-free perovskite-based bifunctional device for both photoelectric conversion and energy storage, *ACS Appl. Energy Mater.* 4 (2021) 7952–7958, <https://doi.org/10.1021/acsaem.1c01272>.
- [22] A.P. Cohn, W.R. Erwin, K. Share, L. Oakes, A.S. Westover, R.E. Carter, R. Bardhan, C.L. Pint, All silicon electrode photocapacitor for integrated energy storage and conversion, *Nano Lett.* 15 (2015) 2727–2731, <https://doi.org/10.1021/acs.nanolett.5b00563>.
- [23] D.C.T. Nguyen, J. Shin, S.K. Kim, S.H. Lee, Solar-powered supercapacitors integrated with a shared electrode, *ACS Appl. Energy Mater.* 4 (2021) 14014–14021, <https://doi.org/10.1021/acsaem.1c02813>.
- [24] C.T. Altaf, A.M. Rostas, M. Mihet, M.D. Lazar, I. Iatsunskiy, E. Coy, E. Erdem, M. Sankir, N.D. Sankir, Solar-assisted all-solid supercapacitors using composite

- nanostructures of ZnO nanowires with GO and rGO, *J. Mater. Chem. C* (2022), <https://doi.org/10.1039/D2TC02114E>.
- [25] C.T. Altaf, T.O. Colak, F. Lufano, G.S. Unal, N.D. Sankir, M. Sankir, Graphitic carbon nitride/zinc oxide composite electrodes for all-solid-state photo-supercapacitor with ion exchange membrane separator, *J. Energy Storage* 55 (2022), 105784, <https://doi.org/10.1016/j.est.2022.105784>.
- [26] J.P. Isaqui, R. Vnekatesan, R. Nagalingam, J. Mayandi, N. Perumal, Bi₂S₃ can do it all: sensitizer, counter electrode, and supercapacitor for symmetric solar cell assisted photo-supercapacitor, *Int. J. Energy Res.* 46 (2022) 11065–11078, <https://doi.org/10.1002/er.7908>.
- [27] W.J. Dong, W.S. Cho, J.L. Lee, Indium tin oxide branched nanowire and Poly(3-hexylthiophene) hybrid structure for a photorechargeable supercapacitor, *ACS Appl. Mater. Interfaces* 13 (2021) 22676–22683, <https://doi.org/10.1021/acsami.1c05241>.
- [28] P. Chen, C. Cao, C. Ding, Z. Yin, S. Qi, J. Guo, M. Zhang, Z. Sun, One-body style photo-supercapacitors based on Ni(OH)₂/TiO₂ heterojunction array: high specific capacitance and ultra-fast charge/discharge response, *J. Power Sources* 521 (2022), 230920, <https://doi.org/10.1016/j.jpowsour.2021.230920>.
- [29] M. Mohsen Momeni, H. Mohammadzadeh Aydisheh, B.-K. Lee, Effectiveness of MnO₂ and V₂O₅ deposition on light fostered supercapacitor performance of WTiO₂ nanotube: novel electrodes for photo-assisted supercapacitors, *Chem. Eng. J.* 450 (2022), 137941, <https://doi.org/10.1016/j.cej.2022.137941>.
- [30] Z. Tang, J. Dai, W. Wei, Z. Gao, Z. Liang, C. Wu, B. Zeng, Y. Xu, G. Chen, W. Luo, C. Yuan, L. Dai, In situ generation of ultrathin MoS₂ nanosheets in carbon matrix for high energy density photo-responsive supercapacitors, *Adv. Sci.* 9 (2022) 2201685, <https://doi.org/10.1002/adv.202201685>.
- [31] E. Salih, M. Mekaway, R.Y.A. Hassan, I.M. El-Sherbiny, Synthesis, characterization and electrochemical-sensor applications of zinc oxide/graphene oxide nanocomposite, *J. Nanostruct. Chem.* 6 (2016) 137–144, <https://doi.org/10.1007/s40097-016-0188-z>.
- [32] Y. Yang, T. Liu, Fabrication and characterization of graphene oxide/zinc oxide nanorods hybrid, *Appl. Surf. Sci.* 257 (2011) 8950–8954, <https://doi.org/10.1016/j.apsusc.2011.05.070>.
- [33] N.A.F. Al-Rawashdeh, O. Allabadi, M.T. Aljarrah, Photocatalytic activity of graphene oxide/zinc oxide nanocomposites with embedded metal nanoparticles for the degradation of organic dyes, *ACS Omega* 5 (2020) 28046–28055, <https://doi.org/10.1021/acsomega.0c03608>.
- [34] Y.-W. Wang, A. Cao, Y. Jiang, X. Zhang, J.-H. Liu, Y. Liu, H. Wang, Superior antibacterial activity of zinc oxide/graphene oxide composites originating from high zinc concentration localized around bacteria, *ACS Appl. Mater. Interfaces* 6 (2014) 2791–2798, <https://doi.org/10.1021/am4053317>.
- [35] K.S. Lee, C.W. Park, S.J. Lee, J.-D. Kim, Hierarchical zinc oxide/graphene oxide composites for energy storage devices, *J. Alloys Compd.* 739 (2018) 522–528, <https://doi.org/10.1016/j.jallcom.2017.12.248>.
- [36] W.K. Chee, H.N. Lim, I. Harrison, K.F. Chong, Z. Zainal, C.H. Ng, N.M. Huang, Performance of flexible and binderless Polypyrrole/Graphene Oxide/Zinc oxide supercapacitor electrode in a symmetrical two-electrode configuration, *Electrochim. Acta* 157 (2015) 88–94, <https://doi.org/10.1016/j.electacta.2015.01.080>.
- [37] G. Guo, L. Huang, Q. Chang, L. Ji, Y. Liu, Y. Xie, W. Shi, N. Jia, Sandwiched nanoarchitecture of reduced graphene oxide/ZnO nanorods/reduced graphene oxide on flexible PET substrate for supercapacitor, *Appl. Phys. Lett.* 99 (2011) 83111, <https://doi.org/10.1063/1.3629789>.
- [38] M. Buldu-Akturk, M. Toufani, A. Tufani, E. Erdem, ZnO and reduced graphene oxide electrodes for all-in-one supercapacitor devices, *Nanoscale* (2022) 3269–3278, <https://doi.org/10.1039/d2nr00018k>.
- [39] H. Kaftekan, R. Ocakoglu, R. Thomann, S. Tu, S. Weber, E. Erdem, EPR and photoluminescence spectroscopy studies on the defect structure of ZnO nanocrystals, *Phys. Rev. B - Condens. Matter Phys.* 86 (2012) 1–9, <https://doi.org/10.1103/PhysRevB.86.014113>.
- [40] D. Chen, Z. Wang, T. Ren, H. Ding, W. Yao, R. Zong, Y. Zhu, Influence of defects on the photocatalytic activity of ZnO, *J. Phys. Chem. C* 118 (2014) 15300–15307, <https://doi.org/10.1021/jp5033349>.
- [41] C.G. Van de Walle, Defect analysis and engineering in ZnO, *Phys. B Condens. Matter* 308–310 (2001) 899–903, [https://doi.org/10.1016/S0921-4526\(01\)00830-4](https://doi.org/10.1016/S0921-4526(01)00830-4).
- [42] S. Nadupalli, S. Repp, S. Weber, E. Erdem, About defect phenomena in ZnO nanocrystals, *Nanoscale* 13 (2021) 9160–9171, <https://doi.org/10.1039/d1nr00943e>.
- [43] S. Najib, F. Bakan, N. Abdullayeva, R. Bahariqushchi, S. Kasap, G. Franzò, M. Sankir, N. Demirci Sankir, S. Mirabella, E. Erdem, Tailoring morphology to control defect structures in ZnO electrodes for high-performance supercapacitor devices, *Nanoscale* 12 (2020) 16162–16172, <https://doi.org/10.1039/d0nr03921g>.
- [44] X. Pan, M.Q. Yang, Y.J. Xu, Morphology control, defect engineering and photoactivity tuning of ZnO crystals by graphene oxide-a unique 2D macromolecular surfactant, *Phys. Chem. Chem. Phys.* 16 (2014) 5589–5599, <https://doi.org/10.1039/c3cp55038a>.
- [45] B. Saini, H.K. D. Laishram, R. Krishnapriya, R. Singhal, R.K. Sharma, Role of ZnO in ZnO nanoflake/Ti₃C₂ MXene composites in photocatalytic and electrocatalytic hydrogen evolution, *ACS Appl. Nano Mater.* 5 (2022) 9319–9333, <https://doi.org/10.1021/acsnanm.2c01639>.
- [46] P. Nandi, D. Das, Photocatalytic degradation of rhodamine-B dye by stable ZnO nanostructures with different calcination temperature induced defects, *Appl. Surf. Sci.* 465 (2019) 546–556, <https://doi.org/10.1016/j.apsusc.2018.09.193>.
- [47] G. Wang, Y. Yang, D. Han, Y. Li, Oxygen defective metal oxides for energy conversion and storage, *Nano Today* 13 (2017) 23–39, <https://doi.org/10.1016/j.nantod.2017.02.009>.
- [48] X. Lu, G. Wang, T. Zhai, M. Yu, J. Gan, Y. Tong, Y. Li, Hydrogenated TiO₂ nanotube arrays for supercapacitors, *Nano Lett.* 12 (2012) 1690–1696, <https://doi.org/10.1021/nl300173j>.
- [49] Y. Tang, Y. Li, W. Guo, J. Wang, X. Li, S. Chen, S. Mu, Y. Zhao, F. Gao, A highly ordered multi-layered hydrogenated TiO₂-II phase nanowire array negative electrode for 2.4 V aqueous asymmetric supercapacitors with high energy density and long cycle life, *J. Mater. Chem. A* 6 (2018) 623–632, <https://doi.org/10.1039/C7TA09590B>.
- [50] M. Yu, H. Sun, X. Sun, F. Lu, G. Wang, T. Hu, H. Qiu, J. Lian, Hierarchical al-doped and hydrogenated ZnO nanowire/MnO₂ ultra-thin nanosheet core/shell arrays for high-performance supercapacitor electrode, *Int. J. Electrochem. Sci.* 8 (2013) 2313–2329.
- [51] J. Chen, Z. Xia, H. Li, Q. Li, Y. Zhang, Preparation of highly capacitive polyaniline/black TiO₂ nanotubes as supercapacitor electrode by hydrogenation and electrochemical deposition, *Electrochim. Acta* 166 (2015) 174–182, <https://doi.org/10.1016/j.electacta.2015.03.058>.
- [52] M. Schumm, ZnO-based semiconductors studied by Raman spectroscopy: semimagnetic alloying, doping, and nanostructures, *Dr. Diss.* (2008) 21–23.
- [53] R. Cuscó, E. Alarcón-Lladó, J. Ibáñez, L. Artús, J. Jiménez, B. Wang, M.J. Callahan, Temperature dependence of raman scattering in ZnO, *Phys. Rev. B* 75 (2007), 165202, <https://doi.org/10.1103/PhysRevB.75.165202>.
- [54] M. Toufani, S. Kasap, A. Tufani, F. Bakan, S. Weber, E. Erdem, Synergy of nano-ZnO and 3D-graphene foam electrodes for asymmetric supercapacitor devices, *Nanoscale* 12 (2020) 12790–12800, <https://doi.org/10.1039/D0NR02028A>.
- [55] S. Claramunt, A. Varea, D. López-Díaz, M.M. Velázquez, A. Cornet, A. Cirera, The importance of interbands on the interpretation of the raman Spectrum of graphene oxide, *J. Phys. Chem. C* 119 (2015) 10123–10129, <https://doi.org/10.1021/acs.jpcc.5b01590>.
- [56] C.T. Altaf, N. Abdullayeva, M. Sankir, N.D. Sankir, CsPbBr₃ and Cs₄PbBr₆-CsPbBr₃ composite perovskite sensitization of 3D-ZnO nanostructures for enhanced photoluminescence emission, *J. Lumin.* 239 (2021), <https://doi.org/10.1016/j.jlumin.2021.118396>.
- [57] D. Damberg, R. Viter, V. Fedorenko, I. Iatsunskyi, E. Coy, O. Graniel, S. Balme, P. Miele, M. Bechelany, Photoluminescence study of defects in ZnO-coated polyacrylonitrile nanofibers, *J. Phys. Chem. C* 124 (2020) 9434–9441, <https://doi.org/10.1021/acs.jpcc.0c00326>.
- [58] N. Abdullayeva, C. Tuc Altaf, A. Kumtepe, N. Yilmaz, O. Coskun, M. Sankir, H. Kurt, C. Celebi, A. Yanilmaz, N. Demirci Sankir, Zinc oxide and metal halide perovskite nanostructures having tunable morphologies grown by nanosecond laser ablation for light-emitting devices, *ACS Appl. Nano Mater.* 3 (2020) 5881–5897, <https://doi.org/10.1021/acsnanm.0c01034>.
- [59] N. Abdullayeva, C.T. Altaf, M. Mintas, A. Ozer, M. Sankir, H. Kurt, N.D. Sankir, Investigation of strain effects on photoelectrochemical performance of flexible ZnO electrodes, *Sci. Rep.* 9 (2019) 1–14, <https://doi.org/10.1038/s41598-019-47546-1>.
- [60] Y. Qi, C. Zhang, S. Liu, Y. Zong, Y. Men, Room-temperature synthesis of ZnO@GO nanocomposites as anode for lithium-ion batteries, *J. Mater. Res.* 33 (2018) 1506–1514, <https://doi.org/10.1557/jmr.2018.110>.
- [61] Y. Gong, D. Li, Q. Fu, C. Pan, Influence of graphene microstructures on electrochemical performance for supercapacitors, *Prog. Nat. Sci. Mater. Int.* 25 (2015) 379–385, <https://doi.org/10.1016/j.pnsc.2015.10.004>.
- [62] Y. Shao, J. Li, Y. Li, H. Wang, Q. Zhang, R.B. Kaner, Flexible quasi-solid-state planar micro-supercapacitor based on cellular graphene films, *Mater. Horiz.* 4 (2017) 1145–1150, <https://doi.org/10.1039/C7MH00441A>.
- [63] J. Liang, G. Zhu, C. Wang, P. Zhao, Y. Wang, Y. Hu, L. Ma, Z. Tie, J. Liu, Z. Jin, An all-inorganic perovskite solar capacitor for efficient and stable spontaneous photocharging, *Nano Energy* 52 (2018) 239–245, <https://doi.org/10.1016/j.nanoen.2018.07.060>.
- [64] A. Roy, P. Majumdar, P. Sengupta, S. Kundu, S. Shinde, A. Jha, K. Pramanik, H. Saha, A photoelectrochemical supercapacitor based on a single BiVO₄-RGO bilayer photocapacitive electrode, *Electrochim. Acta* 329 (2020), 135170, <https://doi.org/10.1016/j.electacta.2019.135170>.
- [65] M. Zhao, Y. Li, F. Lin, Y. Xu, L. Chen, W. Jiang, T. Jiang, S. Yang, Y. Wang, A quasi-solid-state photothermal supercapacitor via enhanced solar energy harvest, *J. Mater. Chem. A* 8 (2020) 1829–1836, <https://doi.org/10.1039/C9TA11793H>.
- [66] I.K. Popoola, M.A. Gondal, A. Popoola, L.E. Oloore, Bismuth-based organometallic halide perovskite photo-supercapacitor utilizing novel polymer gel electrolyte for hybrid energy harvesting and storage applications, *J. Energy Storage* 53 (2022), 105167, <https://doi.org/10.1016/j.est.2022.105167>.
- [67] P.S. Chauhan, S. Kumar, A. Mondal, P. Sharma, M.N. Parekh, V. Panwar, A.M. Rao, A. Misra, Stacked vanadium pentoxide-zinc oxide interface for optically-chargeable supercapacitors, *J. Mater. Chem. A* (2023), <https://doi.org/10.1039/D2TA06790K>.
- [68] D. Solís-Cortés, E. Navarrete-Astorga, R. Schrebl, J.J. Peinado-Pérez, F. Martín, J. R. Ramos-Barrado, E.A. Dalchiele, A solid-state integrated photo-supercapacitor based on ZnO nanorod arrays decorated with Ag₂S quantum dots as the photoanode and a PEDOT charge storage counter-electrode, *RSC Adv.* 10 (2020) 5712–5721, <https://doi.org/10.1039/c9ra10635a>.